Photocatalysis
https://www.sciltp.com/journals/photocatalysis

Article

Metal-Free Conjugated Polyphenothiazine Nanostructures as Visible Light Active Photocatalyst for Selective Aerobic Oxidation of Sulfides

Rituporn Gogoi †,*, Swadhin Kumar Jena †, Astha Singh, Kajal Sharma, Rajesh Kumar and Prem Felix Siril *

School of Chemical Sciences, Indian Institute of Technology Mandi, Kamand, Mandi 175005, HP, India
* Correspondence: hri2porn.gogoi@gmail.com (R.G.); prem@iitmandi.ac.in (P.F.S.)
† These authors contributed equally to this work.

How To Cite: Gogoi, R.; Jena, S.K.; Singh, A.; et al. Metal-Free Conjugated Polyphenothiazine Nanostructures as Visible Light Active Photocatalyst for Selective Aerobic Oxidation of Sulfides. *Photocatalysis* **2026**, *2*(1), 1. https://doi.org/10.53941/photocatalysis.2026.100001

Received: 19 December 2025
Revised: 26 February 2026
Accepted: 10 March 2026
Published: 17 March 2026

Abstract: Phenothiazine (PTZ) and its derivatives have been widely explored for photocatalytic molecular oxygen activation in various chemical transformations due to their high reduction potential. However, their photocatalytic activity is restricted to UV light irradiation because of a wide band gap (~3.56 eV). In this work, we report a single-step polymerization of PTZ to synthesize nanostructured polyphenothiazene (PPTZ). The resulting PPTZ exhibits a significantly reduced band gap (~2 eV), enabling efficient visible-light absorption. Furthermore, polymerization using different oxidizing agents modulates the morphology of PPTZ nanoparticles, leading to distinct photocatalytic performances. As a metal-free photocatalyst, PPTZ nanoparticles demonstrate excellent activity toward the selective aerobic oxidation of sulfides (SAOS) under visible-light irradiation. High sulfide conversions of up to 99% with selectivity exceeding 99% were achieved. Moreover, the photocatalyst is recyclable for at least three consecutive cycles without any significant loss in performance, highlighting PPTZ-based nanomaterials as promising visible-light-active photocatalysts for SAOS reactions.

Keywords: photocatalysis; polyphenothiazine; visible light; arylthiosulfide; sulfoxide

1. Introduction

Selective aerobic oxidation of sulfides (SAOS) is an important chemical transformation for the synthesis of sulfoxides from sulfides. Sulfoxides are the structural components mostly found in a variety of natural products, medications, pesticides, and other useful chemicals. However, their synthesis requires a mild oxidizing agent like molecular oxygen which is a naturally available, priceless and an eco-friendly reagent [1]. However, direct oxidation of organic compounds using molecular oxygen is challenging due to the large energy barrier [2]. Recently, photocatalysis is paid much attention as it requires only a photocatalyst that activates molecular oxygen under sunlight [3–5]. Although, several metal-based photocatalysts are reported [1,6,7], they often cause metallic contamination of the final product, thus increasing production cost through the additional purification steps. Moreover, most of the metallic catalysts have high oxidation potential. Therefore, the reactions that require mild oxidation such as SAOS are overoxidized to sulfones or undesirable side products [2]. Therefore, metal-free photocatalysts are economical and desirable [8].

Phenothiazine (PTZ) and its derivatives have emerged as promising materials in various applications such as solar cells [9], pharmaceutical [10] and photocatalysis. Owing to their tunable electronic structures, photochemical stability and light absorption ability, PTZ showed exceptional activity as metal-free photocatalysts for various application [11–13]. However, PTZ is active mostly in the UV region that covers only a fraction (<5%) of the solar

spectrum [14]. By extending the π-conjugation, small molecules like PTZ can be made to absorb broader solar spectrum. For example, Benzo[b]phenothiazine (Ph-benzoPTZ) performed enhanced photocatalytic conversion than N-phenylphenothiazine (N-PhPTZ) for atom transfer radical polymerization (ATRP) of methyl methacrylate [15]. Ph-benzoPTZ showed broader absorption spectrum with the absorbance maxima shifted to a higher wavelength by 49 nm than N-PhPTZ because of the introduction of an additional phenyl ring. Recently, Jun et al., showed a series of PTZ derivatives up to seven fused phenyl rings for the conversion of primary amines to imines [16]. Conjugated polymers, typically called the conducting polymers can be valuable visible light active metal free photocatalysts. Nanostructuring and nanocomposite formation are some exemplary ways to tune the photocatalytic activities of conducting polymers [17]. For example, porous organic polymers (POP) were used as photocatalysts for the bromoalkylation and cyclopropanation of terminal alkenes [18], while covalent organic frameworks (COF) were employed for the polymerization of methyl methacrylate [19], and oxidative coupling of amines and cyclization of thioamides [20]. However, these materials require complex multiple synthetic steps and require a significant amount of expensive chemicals like metals. Hence, conducting polymer nanostructures (CPNs) received a great deal of attention as visible light active photocatalyst for various applications [21,22]. CPNs have low exciton binding energy and superior charge transport properties. In addition, CPNs can be prepared via chemical oxidative polymerization (COP) in a single-step reaction that reduces time, resources and waste generated, making them perfect for photocatalytic conversions.

In this work, we have synthesized metal-free polyphenothiazines (PPTZ) via one-pot COP of PTZ. We used ammonium persulfate (APS) and benzoyl peroxide (BPO) as oxidants to synthesize metal-free PPTZs (here, PPTZ-APS and PPTZ-BPO respectively). We showed that COP of PTZ transformed UV-active PTZ into visible light active PPTZs that can absorb in a wide range solar spectrum. Also, these CPNs were developed as visible-light-active photocatalysts for the selective aerobic oxidation of sulfides activating molecular oxygen. To the best of our knowledge, this is the first example of using metal-free PPTZ CPNs as visible light active photocatalysts for selective oxidation of sulfides.

2. Experimental

2.1. Materials and Reagents

PTZ (>98% purity) monomer and glacial acetic acid were purchased from central drug house (CDH) Pvt. Ltd. (Gujarat, India). APS (>99% purity) was purchased from Sigma-Aldrich (Bengaluru, Karnataka, India). BPO (>99% purity) was purchased from HiMedia Laboratories Pvt. Ltd. (Mumbai, Maharashtra, India). Sulfides were obtained from Tokyo Chemical Industry (TCI Chemicals) (Hyderabad, Telangana, India). Ultrapure water (Millipore System, 18.2 MΩ cm) was used in the experiments until and unless mentioned otherwise. Acetone, methanol, and hexane were purchased from SD Fine Chemicals Limited (Mumbai, Maharashtra, India). All the reagents are commercially available, analytically pure, and used as received without further purification.

2.2. Synthesis of PPTZ-X Nanoparticles

PPTZ-BPO nanostructures were synthesized by dissolving PTZ (1.99 g, 10 mmol) in acetic acid (50 mL). Benzoyl peroxide (BPO, 4.8 g, 20 mmol) was crushed and added gradually, followed by the addition of water (10 mL) and the reaction mixture was refluxed at 115 °C with constant stirring (300 rpm) for 48 h. After cooling to room temperature, the reaction mixture was diluted to 1 L with deionized water, resulting in the formation of a dark red precipitate. The solid product was collected by centrifugation, washed thoroughly with water, and purified by trituration with n-hexane (three times). The purified material was dried at 60 °C in a hot-air oven to yield PPTZ-BPO nanostructures with an isolated yield of 94%. PPTZ-APS nanostructures were prepared using an analogous procedure, replacing BPO with aqueous solution (10 mL) of APS (4.56 g, 20 mmol), following the reported literature [23].

2.3. Characterization Techniques

A variety of sophisticated techniques were employed to characterize the PPTZ. For the powder X-ray diffraction pattern, Rigaku SmartLab 9 kW rotating anode set with Bragg-Brentano configuration was used. A Cu-sealed tube (Cu K X-rays of 0.1542 nm) was used in the setup, which operated at 100 mA and 45 kV. The scattering patterns were recorded from 10 to 60°, with a scan rate of 2° per minute (step size: 0.02°). Fourier transform infrared spectra (FTIR) were obtained using a Perkin Elmer Spectrum Two coupled with a $LaTiO_3$ MIR detector. The spectra were collected in the range of 4000–400 cm^{-1}. The solid-state NMR spectrum (SS-NMR) was recorded using a Bruker AVANCE HD 500 MHz FT-NMR spectrometer equipped with a 4 mm broadband

CP-MAS solid probe. The samples were loaded into the instrument, which was accommodated inside a zirconia rotor (4 mm). A magnetic field of 11.7 T was applied externally during the analysis. ^{13}C NMR spectra were evaluated using linearly ramped cross-polarization with Magic-angle spinning (CP-MAS) at 125.79 MHz. The CP contact time, flip angle, and pulse width were set to 2 ms, 90°, and 3.84 s, respectively. The material was evaluated with 2048 scans, and a 3 s recycle delay. Thermogravimetric analysis (TGA) was carried out in the temperature range of 25–700 °C using a Perkin Elmer Pyris 1 instrument. The samples were loaded into a Pt crucible and heated at a rate of 5 °C min^{-1} under N_2 gas flow at a rate of 20 mL min^{-1}.

The nitrogen gas adsorption-desorption isotherms at 77 K were recorded in a Quanta chrome Autosorb-iQ-MP/XR system to assess the Brunauer-Emmett-Teller (BET) surface area. Morphology of the particles were imaged using field emission scanning electron microscopy (FESEM, FEI Nova Nano SEM-450). X-ray photoelectron spectra (XPS) were obtained using a Thermo Scientific Nexsa surface analyzer equipped with an Al-k source (with a wavelength of 0.83 nm). The filament current and anode voltage were set to 6.03 mA and 1200 V, respectively. All the spectra were collected with a pass energy of 50 eV and a step size of 0.1 eV. The narrow scan spectra of all the components were deconvoluted using Avantage 5.9908 curve fitting software. For deconvolution, a modified Shirley background was used, with additional constraints applied to keep the background intensity lower than the actual data at any point in the region. As a reference point, adventitious carbon (284.8 eV) was used. Ultraviolet photoelectron spectra (UPS) were obtained by producing ultraviolet photons with He I excitation (21.2 eV). Shimadzu UV-2450 spectrophotometer was used to collect UV-Vis absorbance spectra. On a Horiba flourolog-3, steady-state photoluminescence (PL) emission spectra were recorded using a quartz cell (1 cm) with 5/5 slit widths. The time-resolved fluorescence lifetime was measured with a Horiba Scientific Delta Flex system equipped with a pulsed LED source. The photon decay in various channels was fitted using a bi-exponential equation to obtain lifetime.

The photocatalytic activities were examined under visible light using a custom-built photoreactor made of 160 W white light LED lamps (λ = 400–780 nm, 20 mW cm^{-2}) from Syska. The LED light intensity was measured using a LX-101A digital lux meter. A non-contact digital laser infrared thermometer (HOLDPEAK 320 temperature gun, −30to 320 °C) was used to precisely measure the reaction temperature in the photoreactor. Sulfide conversion and product selectivity were determined using an Agilent 7890A gas chromatography (GC) equipped with a flame ionization detector (FID). A capillary column (19091J-413 HP-5, 30 m, 0.32 mm (ID),) made by Agilent Technology packed with 5% Phenyl methyl polysiloxane was used with high-purity N_2 as the carrier gas. Injector temperature was set at 250 °C, while the detector temperature was 300 °C. The column temperature was raised from 50 °C (hold time = 1.5 min) to 250 °C (hold time = 3 min) at a rate of 20 °C min^{-1}.

2.4. Evaluation of Valence Band

Valence band positions were evaluated from the UPS. Initially, the UPS was calibrated as discussed in the literature [24]. Using the following equation (Equation (1)), the work function (φ) was determined.

$$\varphi = h\nu - (E_f - E_{cut\,off}) \quad (1)$$

where $h\nu$ equals 21.2 eV; (h = Planks constant and ν = frequency) is the source energy, E_f is the fermi energy, and $E_{cut\,off}$ refers to kinetic energy cut off.

2.5. Determination of Optical Band Gap

The Tauc plot was used to analyze the variation of absorptivity ($\alpha h\nu$) as a function of the incident photon energy ($h\nu$). The optical band gap was determined using the Tauc relation given by Equation (2):

$$(\alpha h\nu)^{1/n} = A\,(h\nu - E_g) \quad (2)$$

where 'A' is a proportionality constant, 'α' is the absorption coefficient (α = 2.303 × absorbance), 'h' is Planck's constant, 'ν' is the photon frequency, and 'E_g' represents the optical band gap. The value of 'n' depends on the nature of the electronic transition. For conjugated polymeric semiconductors, n = 1/2, corresponding to a direct allowed transition [25]. The optical band gap was obtained by extrapolating the linear portion of the $(\alpha h\nu)^{1/n}$ vs. $h\nu$ graph at α = 0.

2.6. Steady-State Photoluminescence (PL) and Time-Resolved Emission Spectroscopy (TRES)

At room temperature, steady-state photoluminescence of the materials was measured using Horiba Fluorolog-3 Spectrofluorometer in a quartz cuvette (1 mL) with a path length of 10 mm. For TRES, the materials were analyzed using a Horiba Scientific Delta Flex TCSPC system equipped with pulsed LED sources. To calculate the

instrument response function (IRF), we used LUDOX from Sigma-Aldrich. A bi-exponential fitting of the photon decay profiles was performed with chi-square values ~1.2. The time-resolved fluorescence lifetimes of the materials were obtained according to the mathematical expression (Equation (3)):

$$I = A_1\, exp(-t/\tau_1) + A_2\, exp(-t/\tau_2) \quad (3)$$

In this case, the two-time parameters, τ_1, and τ_2 denote relatively fast and slow recombination processes, respectively. Carrier-carrier scattering or carrier-phonon contact is a part of the faster recombination while the slow recombination processes are radiative recombination transitions of excitons or electron-hole pairs. Two fitted weight variables, A_1 and A_2, correspond to the fast and slow recombination processes, respectively.

2.7. Photoelectrochemical Measurements

An Autolab electrochemical analyzer equipped with a standard three-electrode setup was used to measure transient photocurrent and electrochemical impedance spectroscopy (EIS). The counter electrode was a Pt wire, and the reference electrode was an Ag/AgCl (saturating KCl) electrode. A 100 W LED lamp that was placed 10 cm away from the working electrode was used as a source of illumination. To make the ink, the synthesized materials (5 mg) were thoroughly mixed with Nafion solution (5 wt%, 20 µL) and aqueous IPA (480 µL). The prepared ink was drop-casted on an F-doped SnO_2-coated glass (FTO glass) electrode (1.5 cm × 2.5 cm) with an active area of approximately 1.5 cm^2. The transient photocurrent measurement was carried out with a bias of 0.5 V. The EIS measurements were carried out at a polarization potential of 0.5 V with an AC amplitude of 10 mV and a frequency range of 100 kHz to 0.1 Hz. In both studies, the electrolyte was an aqueous solution of Na_2SO_4 (0.1 M) [26].

2.8. Photocatalytic Activities for Selective Aerobic Oxidation of Sulfides

The selective oxidative properties of the photocatalysts were evaluated for the aerobic oxidation of sulfur. A catalyst dispersion (10 mL, 0.4 mg mL^{-1}) was prepared in methanol using bath sonication for 5 min. The substrate (0.1 mmol) was added to the suspension, sealed with a rubber septum, and saturated with molecular oxygen and maintained by continuous purging from a balloon. The reaction mixture was then placed in the photoreactor for 6 h. After the reaction, the conversion and selectivity of the reaction mixture were analyzed using GC. Retention times of the reactants and products were obtained by injecting commercially available pure compounds. The generalized formulas for conversion and selectivity which uses the peak area of the respective sulfoxide or, sulfide are (Equations (4) and (5) respectively) [27].

$$Conversion\ (\%) = \frac{[Consumed\ sulfide]}{[Initial\ sulfide]} \times 100 \quad (4)$$

$$Selectivity\ (\%) = \frac{[Produced\ sulfoxide]}{[Consumed\ sulfide]} \times 100 \quad (5)$$

3. Results and Discussion

3.1. Synthesis and Characterization

PPTZ were synthesized via COP of PTZ in a single reaction step. We used APS and BPO as oxidizing agents which generate radical cation of PTZ monomer initiating polymeric growth. Polymerisation was evident as the faint greenish-yellow color of PTZ was turned into dark brown as represented in Figure 1a. This indicates the conjugation extension due to polymerization. However, the color change was identical irrespective of the type of oxidizing agent (APS or BPO) used.

Figure 1b shows XRD pattern of the PPTZ along with the PTZ monomer. PTZ shows multiple sharp crystalline peaks specifically in the range 2θ = 15–35°. Interestingly, after polymerization, these peaks disappeared, indicating a decrease in the degree of crystallinity of PTZ [28]. However, PPTZ-BPO showed three minor peaks. These peaks at 12.8, 25, and 27.8 respectively matched well with the (−103), (−215), and (−206) planes of the monoclinic unit cell in PPTZ [29]. FTIR spectra (Figure 1c) were recorded to identify the functional groups present in the materials. PTZ monomer shows a sharp N-H stretching band at 3344 cm^{-1}, which disappears after polymerization due to the involvement of secondary amine (N-H) groups in chain linking, as highlighted in the inset of Figure 1c. In addition, the reduced intensity of the C-H bending vibration at 740 cm^{-1} and the emergence of a weak band at 815 cm^{-1}, attributed to peripheral phenyl groups, provide clear evidence for para-position interlinking of PTZ units through secondary amine groups. The characteristic absorption bands at 1600,

1307–1212, and 1125 cm^{-1} correspond to C=C, C–N, and C–S stretching vibrations, respectively, confirming the preservation of the PTZ backbone after polymerization, regardless of the oxidant used.

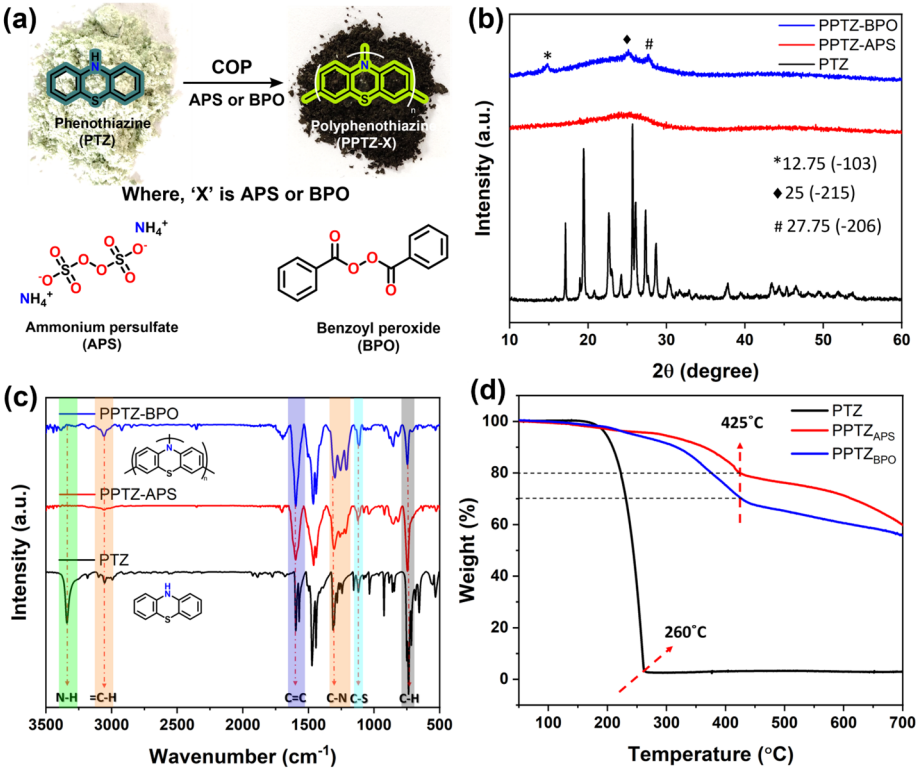

Figure 1. Synthesis and characterizations of PTZ, PPTZ-APS, and PPTZ-BPO: (**a**) general scheme for the synthesis of PPTZ-X, (**b**) powder XRD patterns, (**c**) FTIR spectra and (**d**) TG plots.

This was further confirmed by XPS survey. From Figure S1, the presence of C1s, N1s, and S2p in both PPTZ-APS and PPTZ-BPO is clearly evident. The narrow scan spectra (Figure 2) showed a relatively weak O1s peak at 532.5 eV corresponding to SO_X functional groups including sulfoxide (-SO-) and sulfone ($-SO_2-$). The signal was more intense for PPTZ-APS than PPTZ-BPO. This could be due to the SO_4^{2-} doping from APS. Moreover, S2p spectra of PPTZ-APS showed the presence of SO_4^{2-} groups at 168.5 eV [23]. The presence of C-N-C bonding was clearly identified from the C1s and N1s spectra, as shown in Figure 2. Additionally, the S2p spectra displayed two spin-orbit coupling signals ($S2p_{3/2}$ at 163.4 eV and $S2p_{1/2}$ at 164.6 eV), corresponding to C-S-C linkages. Furthermore, solid-state NMR (SSNMR, Figure 3) of the materials exhibited identical chemical shifts, confirming that the chemical linkages remain unchanged when different oxidizing agents are used.

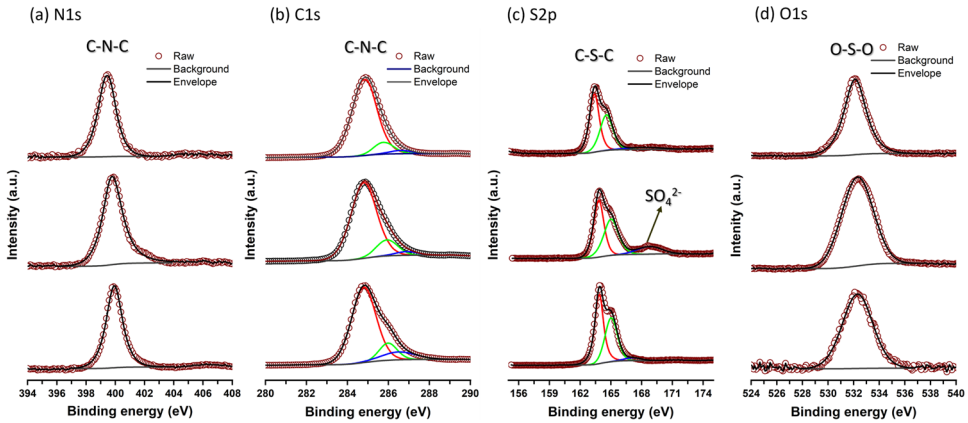

Figure 2. Narrow scan XPS spectra of PTZ (bottom), PPTZ-APS (middle), and PPTZ-BPO (top): (**a**) N1s, (**b**) C1s, (**c**) S2p and (**d**) O1s.

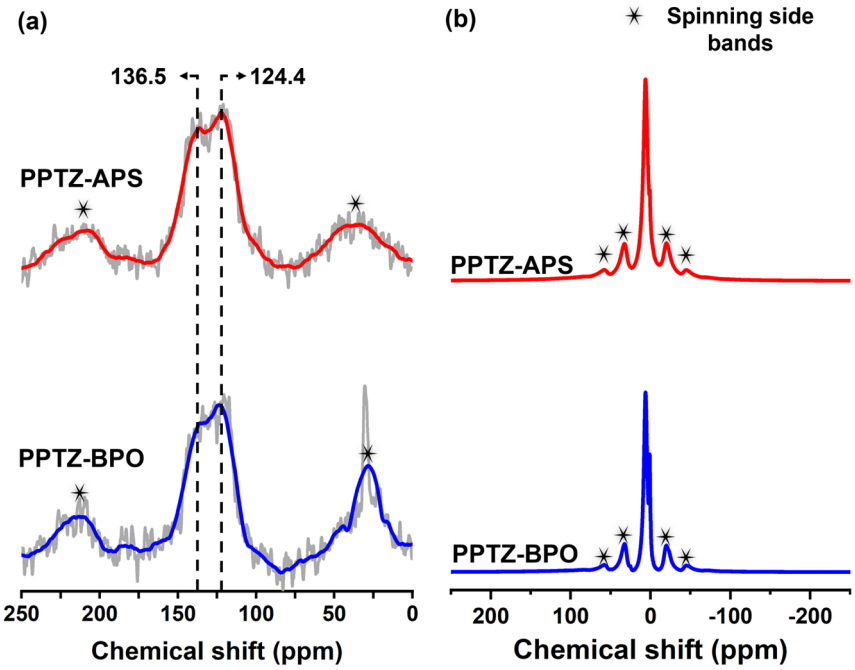

Figure 3. Solid-state NMR (SSNMR) of PPTZ-APS (top) and PPTZ-BPO (bottom): (**a**) ^{13}C SSNMR and (**b**) ^{1}H SSNMR.

The polymers exhibited enhanced thermal stability compared to PTZ, as evident from the TGA thermal curves in Figure 1d. PTZ showed complete mass loss at 260 °C, whereas the polymers demonstrated significantly greater stability. PPTZ-APS and PPTZ-BPO showed only 20% and 30% mass loss, respectively, up to 425 °C.

The morphologies of the nanoparticles were examined using FESEM imaging. PTZ exhibited large rhombus-shaped, two-dimensional (2D) plate-like structures (Figure 4a). On the other hand, the PPTZ formed nanosized particles. PTZ dissolved completely in the reaction medium. PPTZ precipitated out of the solution, because of their poor solubility. PPTZ-APS formed spherical nanoparticles, while PPTZ-BPO exhibited cylindrical shaped nanotubes. The average diameters of the PPTZ-APS and PPTZ-BPO nanoparticles were 272 ± 45 nm and 115 ± 13 nm, respectively (inset, Figure 4b,c).

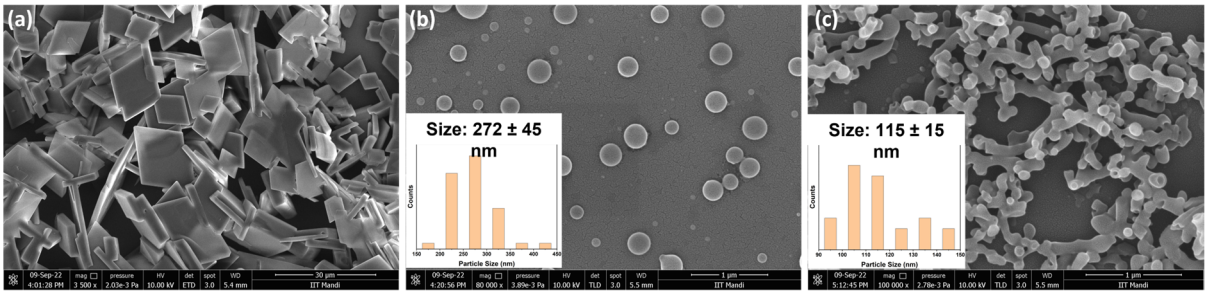

Figure 4. FESEM images of: (**a**) PTZ (scale bar: 30 µm), (**b**) PPTZ-APS (scale bar: 1 µm), and (**c**) PPTZ-BPO (scale bar: 1 µm).

3.2. Photo-, Electro- and Photoelectrochemical Characterization

To investigate the light absorption properties, UV-Vis spectra were recorded. PTZ displayed light absorption in the UV region, as shown in Figure 5a. A sharp absorption peak (λ_{max}) at 252 nm, characteristic of PTZ, was also observed in the PPTZ-X nanostructures. However, polymerization caused a slight red shift (~4 nm) to the λ_{max} of PTZ (left inset, Figure 5a). Additionally, the polymers exhibited broad absorbance in the visible range due to the extended conjugation. As shown in Figure 5b, the polymeric forms displayed PL emission peaks upon excitation at 560 nm, whereas no significant emission was observed for PTZ. This is because PTZ is nearly transparent to visible light. PPTZ-APS showed lower PL intensity than PPTZ-BPO. This may be due to its lower absorbance at 560 nm, which was used to excite the materials.

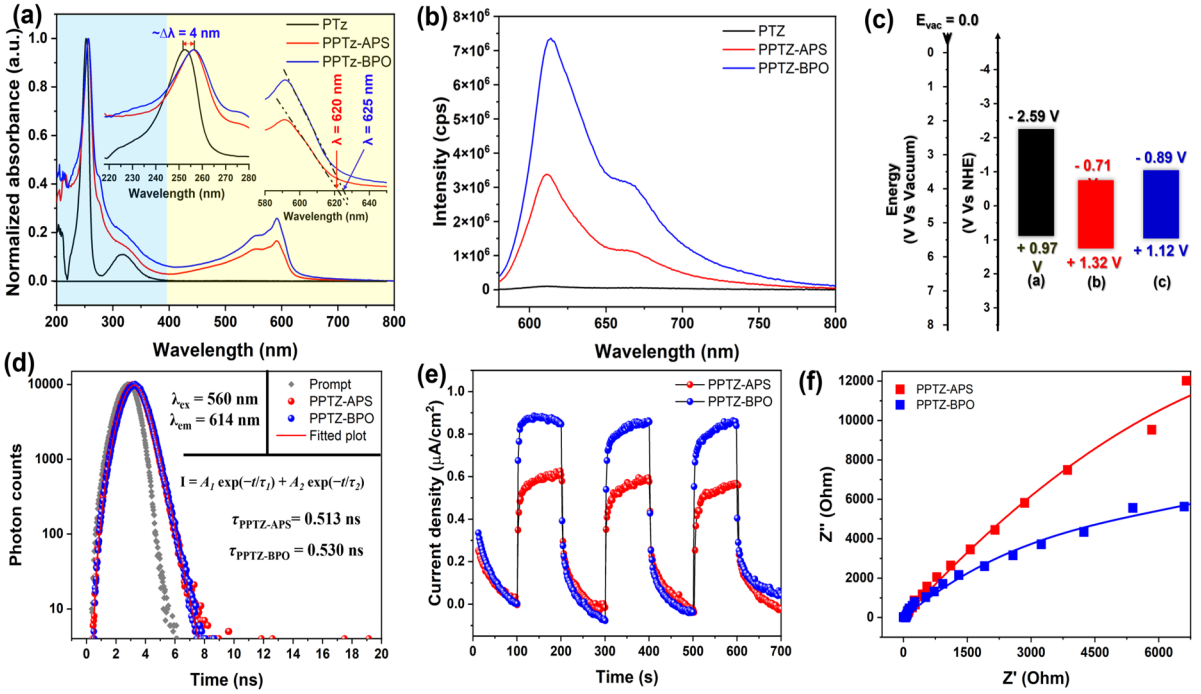

Figure 5. Photo- and photoelectrochemical properties: (**a**) UV-Vis absorbance spectra, (**b**) PL spectra, (**c**) band positions, (**d**) fluorescence lifetime, (**e**) photocurrent, and (**f**) Nyquist plot for EIS spectra.

Further, the Tauc plots shown in Figure 6a were used to determine the optical band gaps of the materials using Equation (2). The measured band gaps of PTZ, PPTZ-APS, and PPTZ-BPO were 3.56, 2.03, and 2.01 eV, respectively. The band gap of PTZ was significantly lowered on polymerization due to the extended conjugation. The valence band maxima (VB_{Max}) of the materials were obtained using UPS measurements under vacuum (Figure 6b). Since 0 V vs. NHE is equivalent to −4.5 eV vs. vacuum, the conduction band maxima (CB_{Max}) of the materials were determined using the empirical formula: $CB_{Min} = VB_{Max} - E_g$. Accordingly, the CB_{Min} values for PTZ, PPTZ-APS, and PPTZ-BPO were found to be −2.59, −0.71, and −0.89 eV, respectively. The various energy band gaps and positions are summarized in Table 1 and Figure 5c.

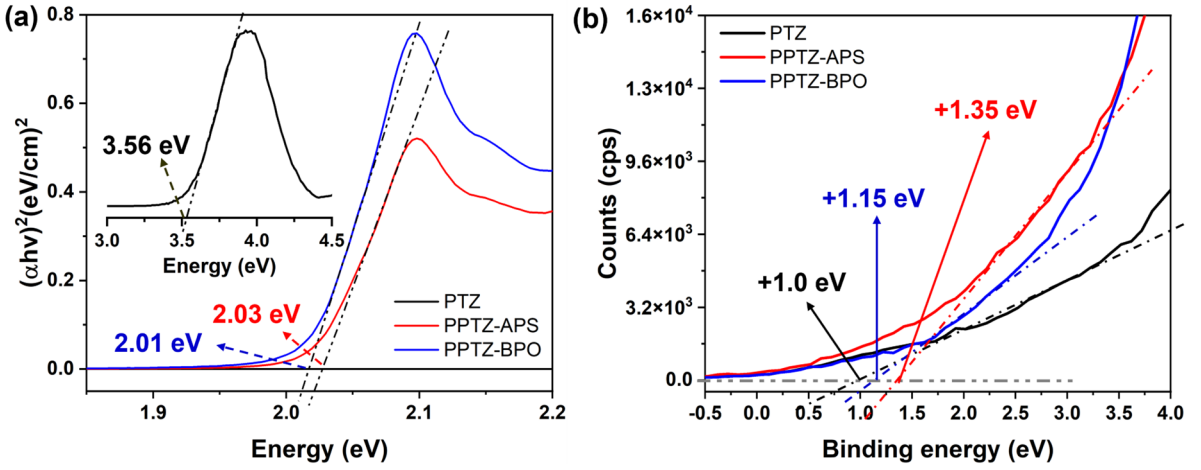

Figure 6. (**a**) Tauc plots showing optical band gaps and (**b**) UPS showing valence band positions.

Table 1. Photophysical properties of PTZ and its polymers.

Materials	Band Gap (E_g)/V vs. NHE	Photoelectrical Energy (eV vs. Ag)			Absolute Energy (eV vs. Vacuum)				Electrochemical Energy (V vs. NHE)	
		Cut Off Energy	Source Energy	φ	VB_{max}	CB_{min}	VB_{max}	CB_{min}	VB_{max}	CB_{min}
PTZ	3.56	16.4	21.22	4.82	+1.00	−2.56	−5.47	−1.91	+0.97	−2.59
PPTZ-APS	2.03	16.4	21.22	4.82	+1.35	−0.68	−5.82	−3.68	+1.32	−0.71
PPTZ-BPO	2.01	16.4	21.22	4.82	+1.15	−0.86	−5.62	−3.61	+1.12	−0.89

The stability of photogenerated charge carriers was assessed using transient lifetime measurements. PPTZ-BPO exhibited a slightly longer lifetime (τ_{BPO} = 0.53 ns) compared to PPTZ-APS (τ_{APS} = 0.51 ns), indicating superior charge carrier separation capability. Additionally, transient photocurrent measurements were conducted by intermittently switching a white LED on and off. As shown in Figure 5e, PPTZ-BPO showed a more intense photocurrent response than PPTZ-APS, highlighting its enhanced optical response and improved charge carrier mobility. However, these measurements could not be performed for PTZ due to its significantly low light absorption in the visible light. This was further validated by EIS measurements. As shown in Figure 5f, PPTZ-BPO exhibited a smaller semi-circular radius compared to PPTZ-APS, indicating lower charge transfer resistance. This indicates the nature of oxidant used for polymerizing PTZ appears to have a significant impact on the photophysical properties of PPTZ nanostructures.

3.3. Evaluation of Photocatalytic Activities for the Selective Aerobic Oxidation of Organic Sulfides (SAOS)

The photophysical properties of the PPTZ motivated us to explore their use as visible-light-active photocatalysts for SAOS. As shown in Table 2, the photocatalytic aerobic oxidation of sulfides could achieve up to 85% conversion within 6 h under visible light irradiation using PPTZ-BPO as the catalyst (Table 2, entry 1). In contrast, no conversion was observed when the reaction was conducted in the absence of visible light (Table 2, entry 2) or without a photocatalyst (Table 2, entry 3). Similarly, the conversion rates were evaluated for PTZ and PPTZ-APS. The photocatalytic activity followed the trend: PTZ < PPTZ-APS < PPTZ-BPO. Both polymeric photocatalysts (PPTZ-BPO and PPTZ-APS) demonstrated excellent photocatalytic activities under visible light, with PPTZ-BPO slightly outperforming PPTZ-APS due to its superior charge separation and more efficient migration of charge carriers. In addition, the BET surface area of the PPTZs was determined using N_2 gas adsorption-desorption isotherms. As shown in Figure S2, PPTZ-BPO exhibited a higher surface area of 4.55 m^2 g^{-1} compared to PPTZ-APS, which has a surface area of 2.88 m^2 g^{-1}. The higher surface area enables high photocatalytic activity in case of PPTz-BPO. Thus, morphology plays a significant role in influencing the photocatalytic activities of PPTZ nanostructures. Furthermore, all the photocatalysts exhibited high selectivity, achieving over 99% sulfoxide production (Table 2, entries 1, 4, and 5). This indicates that polymerization did not alter the intrinsic selectivity of PTZ, though it significantly enhanced the reaction rate.

Table 2. Photocatalytic selective aerobic oxidation of sulfides under visible light. [a]

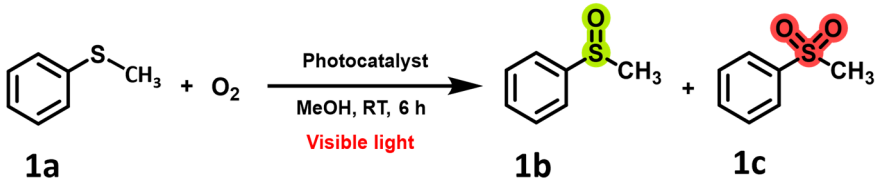

1a 1b 1c

Entry	Catalyst	Conversion (%) [b]	Selectivity (%) [b]
1	PPTZ-BPO	85	99.91
2 [c]	PPTZ-BPO	ND	ND
3	Catalyst free	ND	ND
4	PTZ	2	99.94
5	PPTZ-APS	78	99.97

[a] Reaction conditions: thioanisole (0.1 mmol), photocatalyst (4 mg), CH_3OH (10 mL), O_2 (1 atm), 160 W White LED (λ = 400–780 nm), room temperature, 6 h; [b] Determined by GC; [c] In dark; ND = not detected.

The superior photocatalytic activity of PPTZ is primarily attributed to their enhanced visible-light absorption compared to PTZ. To verify this, the photocatalytic performances of PTZ and PPTZ-BPO were evaluated under UV irradiation (λ ≤ 365 nm), as shown in Figure 7. Both the materials exhibited negligible activity, with sulfide conversions of only 1.2% and 2.6% for PTZ and PPTZ-BPO, respectively. Poor activity of PPTZ-BPO under UV irradiation is expected due to it being visible light active material. However, reason for the poor photocatalytic activity PTZ having UV activity is not very clear. We speculate that the poor catalytic activity of PTZ under UV irradiation may be due to its poor solubility in methanol. In contrast, visible-light irradiation led to a 45-fold enhancement in sulfide conversion for PPTZ-BPO while the activity remained very poor for PTZ, as expected. These results unambiguously demonstrate that polymerization transforms the UV-active PTZ monomer into visible-light-responsive PPTZ-BPO nanostructures, in good agreement with the UV-Vis absorption spectra shown in Figure 5a.

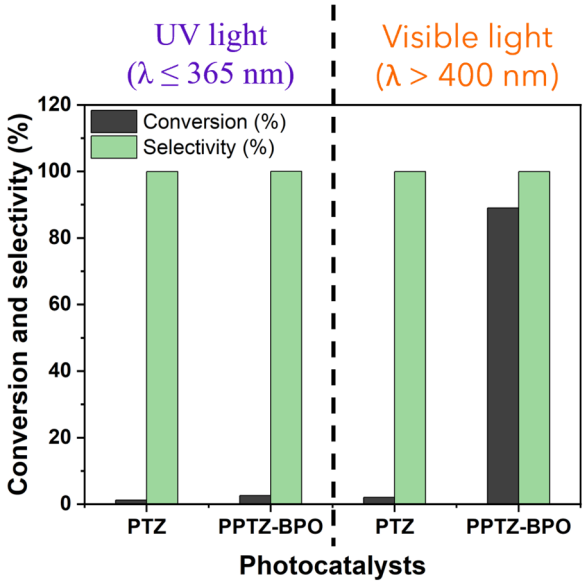

Figure 7. Photocatalytic activities in UV and visible light comparing PTZ and PPTZ-BPO photocatalysts. Reaction conditions: thioanisole (0.1 mmol), photocatalyst (4 mg), CH_3OH (10 mL), O_2 (1 atm), 48 W UV light (λ ≤ 365 nm), or 160 W White LED (λ = 400–780 nm), room temperature, 6 h; conversion was determined by GC analysis.

PPTZ-BPO was further utilized as a photocatalyst for the oxidation of various sulfides to evaluate its substrate scope (Table 3). PPTZ-BPO efficiently converted the substrates regardless of the substituents present. Electron-donating substituents (Table 3, entries 2 and 3) exhibited faster reaction rates compared to electron-withdrawing substituents (Table 3, entry 4) and thioanisole (Table 3, entry 1). Moreover, the photocatalyst demonstrated excellent photocatalytic activity even for sterically hindered substrates. Additionally, it maintained high selectivity across all substrates tested (Table 3, entry 5).

Table 3. Visible light-assisted aerobic oxidation of various sulfides using PPTZ-BPO photocatalyst. [a]

Entry	Substrate	Product	Time (h)	Conversion (%) [b]	Selectivity (%) [b]
1	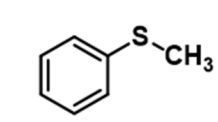	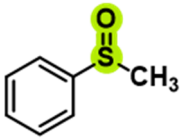	6	85	99.9
2	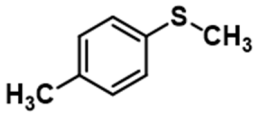	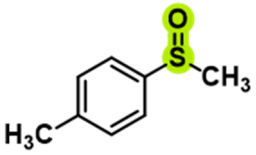	5	99.1	99.2
3	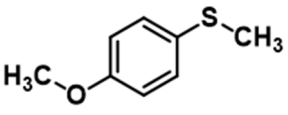	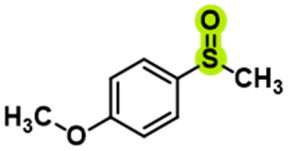	4	100	100
4	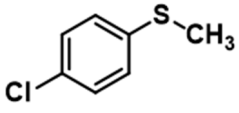	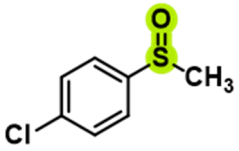	6	76.3	99.2
5	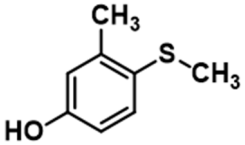	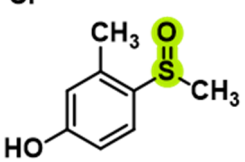	4	98	99.9

[a] Reaction conditions: thioanisole (0.1 mmol), photocatalyst (4 mg), CH_3OH (10 mL), O_2 (1 atm), 160 W White LED (λ = 400–780 nm), room temperature; [b] Determined by GC.

The photocatalytic activity of PPTZ-BPO was compared with a range of metal-free photocatalysts reported over the past few years, as summarized in Table S1. A direct quantitative comparison is difficult due to variations in experimental parameters such as light source, reaction system, catalyst loading, and evaluation methods. PPTZ-BPO exhibited better catalytic activities than many of the reported catalysts on a mass activity basis. Notably, high selectivity was maintained across different photocatalysts employed for the SAOS reactions, regardless of the solvent or catalyst.

Photogenerated reactive species facilitate oxidation, reduction, or both processes. To gain mechanistic insights into the excellent photocatalytic activities, several radical trapping experiments were conducted. Scavenging agents selectively block certain radical pathways, resulting in variation of reaction rates compared to the control reaction, allowing their roles to be identified. The relative conversion of thioanisole in the presence and absence of various scavenging agents was evaluated, as shown in Figure 8a. The roles of reactive oxygen species (ROSs), including superoxide ($O_2^{\bullet-}$), singlet oxygen ($^1O_2$), and hydroxyl radicals ($^{\bullet}OH$), were investigated. The reaction conversion decreased significantly to ~48% in the presence of p-benzoquinone (p-BQ), which traps $O_2^{\bullet-}$, preventing it from participating in the oxidation reaction. Similarly, the conversion dropped to ~36% with the addition of TEMPO, a singlet oxygen ($^1O_2$) scavenger. Furthermore, when the reaction was conducted under a nitrogen atmosphere, the conversion was significantly reduced to ~21%. Nitrogen purging flushes out oxygen present in the reaction mixture. Overall, the above studies clearly indicate that the sulfur conversion is primarily driven by an aerobic photocatalytic process. To investigate the role of hydroxyl radicals ($^{\bullet}OH$), we employed t-BuOH as a scavenging agent. However, no change in the reaction rate was observed. Thus, there seems to be no involvement of $^{\bullet}OH$ radicals. The apparent selectivity in sulfide oxidation is attributed to the absence of $^{\bullet}OH$ radicals, which possess the highest standard oxidation potential of +2.8 V (vs. SHE). Hydroxyl radicals are non-selective, reacting indiscriminately with nearly all substrates [30].

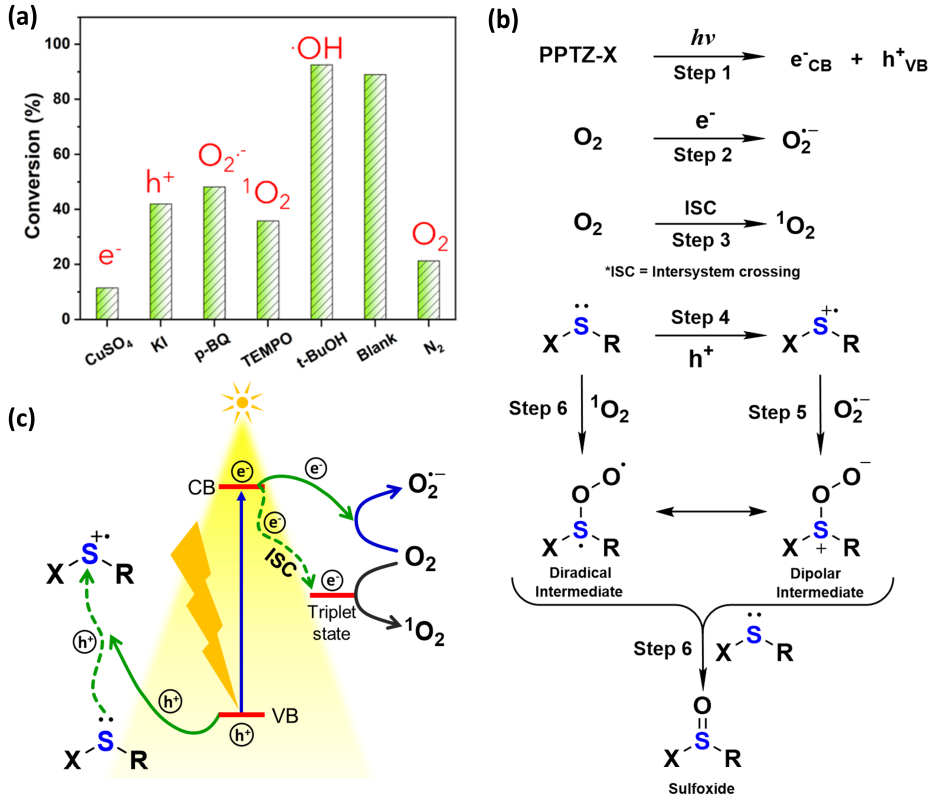

Figure 8. Evaluation of the plausible reaction mechanism: (**a**) effects of various scavengers on the selective oxidation of sulfides under visible light, (**b**) various chemical pathways, and (**c**) schematic representation of the proposed mechanism. Reaction conditions: thioanisole (0.1 mmol), photocatalyst (4 mg), CH_3OH (10 mL), O_2 (1 atm), 160 W White LED (λ = 400–780 nm), room temperature, 6 h; Conversion was determined by GC.

The transfer of electrons to molecular oxygen is crucial for generating $O_2^{\bullet-}$ and $^1O_2$ species. To investigate this, $CuSO_4$ was used as an electron scavenger, which resulted in the most significant suppression of the oxidation rate, reducing the conversion to mere ~11%. The CB_{min} of PPTZ-BPO is −0.89 V vs. NHE which is more negative than the standard reduction potential for molecular oxygen to $O_2^{\bullet-}$ which is −0.33 V vs. NHE. Thus, the band

position of PPTZ-BPO is suitable to drive this reaction. Additionally, the photocatalytic SAOS decreased to ~42% when KI was employed as a hole scavenger, confirming the critical role of photogenerated holes. Based on these findings, the overall mechanism for the photocatalytic oxidation reaction is summarized in Figure 8b,c.

The photocatalyst (PPTZ-BPO) absorbs visible light and becomes excited, generating electrons and holes (Step 1). However, a small fraction of these charge carriers recombines during this initial step. The remaining stable charge carriers diffuse to the surface of the photocatalyst. The excited electrons are then transferred to O_2, resulting in the formation of $O_2^{\bullet-}$ anion radicals (Step 2). The contribution of $^1O_2$ is also significant, as indicated by the scavenging studies. Thus, an energy transfer from the triplet state likely occurs, facilitating the formation of $^1O_2$ (Step 3). Alternatively, photogenerated holes can directly oxidize sulfides into their corresponding sulfoxides (Step 4). The holes generate sulfur-centered free radical cations, which promote easier oxidation to the final products [27]. The $O_2^{\bullet-}$ species, together with the sulfur-centered free radical cations, can form dipolar intermediates, such as peroxysulfoxide (Step 5). Meanwhile, $^1O_2$ directly interacts with the substrates, producing diradical intermediates (Step 6). These intermediates coexist and subsequently react with sulfide molecules, leading to the selective formation of sulfoxides.

Recyclability and reusability are key indicators of the practical viability, cost-effectiveness, and long-term stability of a heterogeneous catalyst [31,32]. Hence, recyclability of PPTZ-BPO was tested under the optimized conditions. PPTZ-BPO could be recovered easily and reused for three consecutive cycles without any noticeable loss in catalytic conversion and selectivity (Figure S3). Even after the 3rd cycle, PPTZ-BPO retained its initial catalytic activity. Furthermore, XRD and FTIR analyses were performed after the 3rd cycle to examine any possible structural changes (Figure S4). No significant changes were observed, confirming the structural stability and superior applicability of PPTZ-BPO for the SAOS reaction.

4. Conclusions

In conclusion, we synthesized polyphenothiazine nanostructures via a one-pot chemical oxidative polymerization of the phenothiazine. This polymerization converts UV-active phenothiazine into visible-light-active conjugated PPTZ. The morphology of PPTZ can be tailored by the choice of oxidants, yielding spherical nanostructures with APS and cylindrical nanostructures with BPO. The resulting PPTZ materials efficiently activate molecular oxygen as a mild oxidant and drive selective aerobic oxidation of sulfides under visible-light irradiation. Notably, PPTZ exhibits up to a 45-fold enhancement in photocatalytic activity relative to the PTZ monomer owing to the enhanced visible-light absorption and improved charge separation. Furthermore, the PPTZ photocatalysts are readily recoverable and reusable for at least three cycles without noticeable loss of activity. Overall, this work establishes PPTZ as a sustainable, metal-free photocatalyst for visible-light-driven green selective aerobic oxidation reactions for sulfides.

Supplementary Materials

The additional data and information can be downloaded at: https://media.sciltp.com/articles/others/2603171724005544/Photocatalysis-25120154-SI-FC.pdf. Figure S1: XPS survey spectra of PTZ, PPTZ-APS, and PPTZ-BPO. Figure S2: Surface area analysis of (**a**) PPTZ-APS and (**b**) PPTZ-APS. Figure S3: Recyclability test up to 3 cycles. Reaction conditions: thioanisole (0.1 mmol), photocatalyst (4 mg), CH_3OH (10 mL), O_2 (1 atm), 160 W White LED (λ = 400–780 nm), room temperature, 6 h; Conversion was determined by GC. Figure S4: Characterization of PPTZ-BPO after the third recyclability test: (**a**) FTIR and (**b**) XRD. Table S1: Comparison of the photocatalytic performance of PPTZ-BPO with recently reported photocatalysts for SAOS reactions using thioanisole as substrate. References [33–42] are cited in the supplementary materials.

Author Contributions

R.G.: Conceptualization, methodology, software, writing—original draft, investigation, S.K.J.: writing—original draft, Formal analysis, methodology, data curation, software; A.S.: methodology, visualization, investigation; K.S.: formal analysis, methodology, visualization, R.K.: Visualization, Validation, P.F.S.: supervision, validation, writing—reviewing and editing, Funding acquisition and Project administration. All authors have read and agreed to the published version of the manuscript.

Funding

The Scheme for Promotion of Academic and Research Collaboration (SPARC, Project p-32), Ministry of Education (MoE), Government of India (GoI).

Institutional Review Board Statement

Not applicable.

Informed Consent Statement

Not applicable.

Data Availability Statement

Data will be made available on request.

Acknowledgments

Rituporn Gogoi, Swadhin Kumar Jena, Astha Singh, and Kajal Sharma acknowledge Ministry of Education (MoE) for HTRA fellowship. The authors specially acknowledge the financial support from SPARC and Advanced Material Research Centre (AMRC), IIT Mandi for research facilities.

Conflicts of Interest

The authors declare no conflict of interest.

Use of AI and AI-Assisted Technologies

During the preparation of this work, the authors used ChatGPT 5.2 to improve readability and language. After using this tool/service, the authors reviewed and edited the content as needed and take full responsibility for the content of the publication.

References

1. Li, Q.; Li, F. Recent Advances in Molecular Oxygen Activation via Photocatalysis and Its Application in Oxidation Reactions. *Chem. Eng. J.* **2021**, *421*, 129915. https://doi.org/10.1016/j.cej.2021.129915.
2. Liu, K.-J.; Deng, J.-H.; Yang, J.; et al. Selective Oxidation of (Hetero)Sulfides with Molecular Oxygen under Clean Conditions. *Green Chem.* **2020**, *22*, 433–438. https://doi.org/10.1039/C9GC03713F.
3. Zhao, L.; Yang, P.; Shi, S.; et al. Activation of Molecular Oxygen for Alcohol Oxidation over Vanadium Carbon Catalysts Synthesized via the Heterogeneous Ligand Strategy. *ACS Catal.* **2022**, *12*, 15249–15258. https://doi.org/10.1021/acscatal.2c04601.
4. Dang, X.; Yang, R.; Wang, Z.; et al. Efficient Visible-Light Activation of Molecular Oxygen to Produce Hydrogen Peroxide Using P Doped g-C_3N_4 Hollow Spheres. *J. Mater. Chem. A* **2020**, *8*, 22720–22727. https://doi.org/10.1039/D0TA07794A.
5. Gogoi, R.; Jena, S.K.; Singh, A.; et al. Mechanically Pulverized Covalent Organic Framework as a Metal-Free Photocatalyst for Fenton-like Degradation of Organic Pollutants and Hexavalent Chromium Reduction. *J. Environ. Chem. Eng.* **2024**, *12*, 112006. https://doi.org/10.1016/J.JECE.2024.112006.
6. Casado-Sánchez, A.; Gómez-Ballesteros, R.; Tato, F.; et al. Pt(II) Coordination Complexes as Visible Light Photocatalysts for the Oxidation of Sulfides Using Batch and Flow Processes. *Chem. Commun.* **2016**, *52*, 9137–9140. https://doi.org/10.1039/C6CC02452A.
7. Lang, X.; Zhao, J.; Chen, X. Visible-Light-Induced Photoredox Catalysis of Dye-Sensitized Titanium Dioxide: Selective Aerobic Oxidation of Organic Sulfides. *Angew. Chem. Int. Ed.* **2016**, *55*, 4697–4700. https://doi.org/10.1002/ANIE.201600405.
8. Serviou, S.K.; Gkizis, P.L.; Sánchez, D.P.; et al. Expanding the Use of Benzothioxanthene Imides to Photochemistry: Eco-Friendly Aerobic Oxidation of Sulfides to Sulfoxides. *ChemSusChem* **2024**, *17*, e202400903. https://doi.org/10.1002/cssc.202400903.
9. Elanthendral, M.; Vennila, P.; Venkatesh, G. Design, Synthesis, and Photo Physical Characterization of Phenyl-(Benzo) Phenothiazine-Based Organic Photosensitizes for Dye-Sensitized Solar Cells. *J. Phys. Chem. Solids* **2026**, *208*, 113010. https://doi.org/10.1016/j.jpcs.2025.113010.
10. Bandishti, M.; Pramanik, C.; Roychowdury, A.; et al. A Concise Review of Phenothiazine Based Antipsychotic Drugs and Their Syntheses. *J. Heterocycl. Chem.* **2026**, *63*, 106–129. https://doi.org/10.1002/jhet.70115.
11. Park, J.H.; Ko, K.C.; Kim, E.; et al. Photocatalysis by Phenothiazine Dyes: Visible-Light-Driven Oxidative Coupling of Primary Amines at Ambient Temperature. *Org. Lett.* **2012**, *14*, 5502–5505. https://doi.org/10.1021/ol302584y.
12. Discekici, E.H.; Treat, N.J.; Poelma, S.O.; et al. A Highly Reducing Metal-Free Photoredox Catalyst: Design and Application in Radical Dehalogenations. *Chem. Commun.* **2015**, *51*, 11705–11708. https://doi.org/10.1039/C5CC04677G.

13. Ando, H.; Takamura, H.; Kadota, I.; et al. Strongly Reducing Helical Phenothiazines as Recyclable Organophotoredox Catalysts. *Chem. Commun.* **2024**, *60*, 4765–4768. https://doi.org/10.1039/D4CC00904E.
14. Wang, X.; Wang, F.; Sang, Y.; et al. Full-Spectrum Solar-Light-Activated Photocatalysts for Light–Chemical Energy Conversion. *Adv. Energy Mater.* **2017**, *7*, 1700473. https://doi.org/10.1002/aenm.201700473.
15. Dadashi-Silab, S.; Pan, X.; Matyjaszewski, K. Phenyl Benzo[b]Phenothiazine as a Visible Light Photoredox Catalyst for Metal-Free Atom Transfer Radical Polymerization. *Chem. A Eur. J.* **2017**, *23*, 5972–5977. https://doi.org/10.1002/chem.201605574.
16. Zhou, J.; Mao, L.; Wu, M.-X.; et al. Extended Phenothiazines: Synthesis, Photophysical and Redox Properties, and Efficient Photocatalytic Oxidative Coupling of Amines. *Chem. Sci.* **2022**, *13*, 5252–5260. https://doi.org/10.1039/D2SC01086K.
17. Gogoi, R.; Dutt, S.; Siril, P.F. Conjugated Polymer-Based Nanocomposites as Photocatalysts. In *Conjugated Polymers Nanostructures for Energy Conversion and Storage Applications*; Wiley: Hoboken, NJ, USA, 2021; pp 267–296. https://doi.org/10.1002/9783527820115.CH8.
18. Wang, R.; Zhou, C.; Huang, X.; et al. Phenylphenothiazine-Based Porous Organic Polymers as Visible-Light Heterogeneous Photocatalysts for Switchable Bromoalkylation and Cyclopropanation of Unactivated Terminal Alkenes. *ACS Sustain. Chem. Eng.* **2022**, *10*, 4650–4659. https://doi.org/10.1021/acssuschemeng.2c00054.
19. Wang, W.; Wang, H.; Tang, X.; et al. Phenothiazine-Based Covalent Organic Frameworks with Low Exciton Binding Energies for Photocatalysis. *Chem. Sci.* **2022**, *13*, 8679–8685. https://doi.org/10.1039/D2SC02503E.
20. Liu, Y.; Jiang, X.; Chen, L.; et al. Rational Design of a Phenothiazine-Based Donor–Acceptor Covalent Organic Framework for Enhanced Photocatalytic Oxidative Coupling of Amines and Cyclization of Thioamides. *J. Mater. Chem. A* **2023**, *11*, 1208–1215. https://doi.org/10.1039/D2TA07177K.
21. Ghosh, S.; Kouamé, N.A.; Ramos, L.; et al. Conducting Polymer Nanostructures for Photocatalysis under Visible Light. *Nat. Mater.* **2015**, *14*, 505–511. https://doi.org/10.1038/nmat4220.
22. Gogoi, R.; Singh, A.; Moutam, V.; et al. Revealing the Unexplored Effect of Residual Iron Oxide on the Photoreforming Activities of Polypyrrole Nanostructures on Plastic Waste and Photocatalytic Pollutant Degradation. *J. Environ. Chem. Eng.* **2022**, *10*, 106649. https://doi.org/10.1016/j.jece.2021.106649.
23. Wang, X.; Li, G.; Han, Y.; et al. Facile Synthesis of Polyphenothiazine as a High-Performance p-Type Cathode for Rechargeable Lithium Batteries. *ChemSusChem* **2021**, *14*, 3174–3181. https://doi.org/10.1002/cssc.202101008.
24. Maheu, C.; Cardenas, L.; Puzenat, E.; et al. UPS and UV Spectroscopies Combined to Position the Energy Levels of TiO_2 Anatase and Rutile Nanopowders. *Phys. Chem. Chem. Phys.* **2018**, *20*, 25629–25637. https://doi.org/10.1039/C8CP04614J.
25. Khoirun Nisa, Q.A.; Son, D.H.; Kim, J.H. A Step-by-Step Strategy to Enhancing the Photovoltaic Performance of Indandione-Based Polymers. *Dye. Pigment.* **2022**, *207*, 110760. https://doi.org/10.1016/j.dyepig.2022.110760.
26. Singh, A.; Jena, S.K.; Siril, P.F.; et al. COFfee: A Coffee Waste@Anthraquinone COF Nanocomposite as a Photocatalyst for Green Hydrogen Production. *ACS Sustain. Resour. Manag.* **2026**, *3*, 45–51. https://doi.org/10.1021/acssusresmgt.5c00454.
27. Li, Q.; Lan, X.; An, G.; et al. Visible-Light-Responsive Anthraquinone Functionalized Covalent Organic Frameworks for Metal-Free Selective Oxidation of Sulfides: Effects of Morphology and Structure. *ACS Catal.* **2020**, *10*, 6664–6675. https://doi.org/10.1021/acscatal.0c00290.
28. Yang, Y.; Chen, M.; Li, H.; et al. The Degree of Crystallinity Exhibiting a Spatial Distribution in Polymer Films. *Eur. Polym. J.* **2018**, *107*, 303–307. https://doi.org/10.1016/j.eurpolymj.2018.08.041.
29. Korolev, Y.M.; Ozkan, S.Z. Synthesis and X-Ray Diffraction Study of Polyphenothiazine. *Dokl. Phys. Chem.* **2009**, *429*, 223–226. https://doi.org/10.1134/S0012501609110025.
30. Wang, X.; Zhang, L. Kinetic Study of Hydroxyl Radical Formation in a Continuous Hydroxyl Generation System. *RSC Adv.* **2018**, *8*, 40632–40638. https://doi.org/10.1039/C8RA08511K.
31. Gogoi, R.; Dohling, H.M.; Singh, A.; et al. Visible Light Enhanced Photosynthesis of C-C Bonds Using PdO/Pd@PEDOT Nanocomposite. *J. Catal.* **2022**, *414*, 109–124. https://doi.org/10.1016/j.jcat.2022.08.027.
32. Singh, A.; Surial, S.; Jena, S.K.; et al. Sulfone Based Conjugated Porous Organic Polymer-Immobilized Electrospun Nanofibers for Continuous-Flow Photoreduction of Hexavalent Chromium. *Chem. Eng. J. Adv.* **2026**, *2*, 100026. https://doi.org/10.1016/j.cejgas.2026.100026.
33. Zhao, Z.Y.; Wang, S.J.; Mi, L.B.; et al. Perylene Diimide-Based Hyper-Cross-Linked Polymers for Visible-Light-Driven Selective Organic Sulfide Oxidation. *Sep. Purif. Technol.* **2025**, *359*, 130543. https://doi.org/10.1016/J.SEPPUR.2024.130543.
34. Dong, X.; Xu, H.; Hao, H.; et al. Selective Photocatalytic Oxidation of Sulfides with Dioxygen over Carbazole–Fluorene Conjugated Microporous Polymers. *J. Colloid Interface Sci.* **2022**, *608*, 882–892. https://doi.org/10.1016/J.JCIS.2021.10.047.
35. Zhang, F.; Ma, X.; Dong, X.; et al. Inserting Acetylene into an Olefin-Linked Covalent Organic Framework for Boosting the Selective Photocatalytic Aerobic Oxidation of Sulfides. *Chem. Eng. J.* **2023**, *451*, 138802. https://doi.org/10.1016/J.CEJ.2022.138802.
36. Ji, G.; Yang, Z.; Yu, X.; et al. Photosensitive Hyper-Cross-Linked Polymers Derived from Three-Dimensional Ringlike Arenes: Promising Catalysts for Singlet-Oxygen Generation. *ACS Sustain. Chem. Eng.* **2020**, *8*, 16320–16326. https://doi.org/10.1021/acssuschemeng.0c06025.

37. Shan, H.; Zhang, Z.; Jiang, Y.; et al. Two-Dimensional Porphyrin-Based Covalent Organic Frameworks for Heterogeneous Photocatalysis: Influence of Pore Size on Photocatalytic Performance. *Sep. Purif. Technol.* **2025**, *363*, 132102. https://doi.org/10.1016/J.SEPPUR.2025.132102.
38. Xie, Q.; Chen, A.; Gao, Z.; et al. Regulating Conformational Locking in Covalent Organic Framework for Selective and Recyclable Photocatalytic Transformation. *Small* **2024**, *20*, 2405550. https://doi.org/10.1002/smll.202405550.
39. Lei, H.; Zhu, C.; Lin, L.; et al. Rational Modulation of Covalent Organic Frameworks Heterogeneous Catalyst: Structural Cationization Effect on Accelerating Photocatalytic Oxidation Process. *Appl. Catal. B Environ. Energy* **2025**, *361*, 124654. https://doi.org/10.1016/J.APCATB.2024.124654.
40. Wang, Z.; Qi, Z.; Wang, S.; et al. Porphyrin Based Covalent Organic Frameworks via Self-Polycondensation for Heterogeneous Photocatalysis. *J. Colloid Interface Sci.* **2025**, *683*, 736–745. https://doi.org/10.1016/J.JCIS.2024.12.205.
41. Zhang, H.; Huang, Q.; Zhang, W.; et al. Benzodithiophenedione-Based Conjugated Microporous Polymer Catalysts for Aerobic Oxidation Reactions Driven by Visible-Light. *ChemPhotoChem* **2019**, *3*, 645–651. https://doi.org/10.1002/CPTC.201900095.
42. Dong, X.; Huang, F.; Wang, Y.; et al. Selective Oxidation of Sulfides by Pyrene-π-Anthraquinone Conjugated Microporous Polymer Photocatalysis. *Mater. Today Energy* **2023**, *38*, 101443. https://doi.org/10.1016/J.MTENER.2023.101443.